

Open Research Online

The Open University's repository of research publications
and other research outputs

Enhanced Super-Rotation Before and During the 2018 Martian Global Dust Storm

Journal Item

How to cite:

Rajendran, Kylash; Lewis, Stephen; Holmes, James; Streeter, Paul; Fedorova, Anna and Patel, Manish (2021). Enhanced Super-Rotation Before and During the 2018 Martian Global Dust Storm. *Geophysical Research Letters*, 48(16), article no. e2021GL094634.

For guidance on citations see [FAQs](#).

© 2021 The Authors.



<https://creativecommons.org/licenses/by/4.0/>

Version: Version of Record

Link(s) to article on publisher's website:

<http://dx.doi.org/doi:10.1029/2021GL094634>

Copyright and Moral Rights for the articles on this site are retained by the individual authors and/or other copyright owners. For more information on Open Research Online's data [policy](#) on reuse of materials please consult the policies page.

oro.open.ac.uk

Geophysical Research Letters



RESEARCH LETTER

10.1029/2021GL094634

Key Points:

- The martian atmosphere was already in a state of enhanced super-rotation prior to the onset of the Mars Year 34 global dust storm
- Super-rotation doubled during the peak of the storm and tropical easterlies were strongly enhanced above 60 km
- Dust lifting in the southern hemisphere led to enhanced tropical heating and increased vertical dust transport in the lead-up to the storm

Correspondence to:

K. Rajendran,
kylash.rajendran@open.ac.uk

Citation:

Rajendran, K., Lewis, S. R., Holmes, J. A., Streeter, P. M., Fedorova, A. A., & Patel, M. R. (2021). Enhanced super-rotation before and during the 2018 martian global dust storm. *Geophysical Research Letters*, 48, e2021GL094634. <https://doi.org/10.1029/2021GL094634>

Received 4 DEC 2020
 Accepted 23 JUL 2021

Enhanced Super-Rotation Before and During the 2018 Martian Global Dust Storm

Kylash Rajendran¹ , Stephen R. Lewis¹ , James A. Holmes¹ , Paul M. Streeter¹ , Anna A. Fedorova² , and Manish R. Patel^{1,3}

¹School of Physical Sciences, The Open University, Milton Keynes, UK, ²Space Research Institute of the Russian Academy of Sciences (IKI RAS), Moscow, Russia, ³Space Science and Technology Department, Science and Technology Facilities Council, Rutherford Appleton Laboratory, Oxfordshire, UK

Abstract Super-rotation affects—and is affected by—the distribution of dust in the martian atmosphere. We modeled this interaction during the 2018 global dust storm (GDS) of Mars Year 34 using data assimilation. Super-rotation increased by a factor of two at the peak of the GDS, as compared to the same period in the previous year which did not feature a GDS. A strong westerly jet formed in the tropical lower atmosphere, with strong easterlies above 60 km, as a result of momentum transport by thermal tides. Enhanced super-rotation is shown to have commenced 40 sols before the onset of the GDS, due to dust lifting in the southern mid-latitudes and tropics. The uniform distribution of dust in the tropics resulted in a symmetric Hadley cell with a tropical upwelling branch that could efficiently transport dust vertically; this may have significantly contributed to the rapid expansion of the storm.

Plain Language Summary Dust plays a major role in driving the behavior of the atmosphere of Mars. During a global dust storm (GDS), winds lift, and transport dust throughout the atmosphere; in turn, dust affects wind direction and strength by heating and cooling the surrounding air. Using a technique that combines satellite observations with simulations of the martian atmosphere, we demonstrate that winds at tropical latitudes were greatly strengthened during the 2018 GDS as a result of heating by dust. We show that tropical winds were strengthened even before the onset of the storm, as a result of a dust-driven modification to the tropical circulation pattern. This change in the tropical circulation may have played a role in the formation of the GDS.

1. Introduction

A planetary atmosphere is said to be in a state of *super-rotation* if the total axial angular momentum of the atmosphere is greater than the angular momentum of an atmosphere in a state of pure solid-body rotation (Read, 1986). Super-rotation usually takes the form of an equatorial jet directed in the same sense as the planet's rotation, and it has been shown that such a state can only be maintained by the equatorward transport of angular momentum by non-axisymmetric eddy motions (Hide, 1969). Identifying the exact mechanisms that initiate and maintain super-rotating jets remains a significant challenge in planetary atmospheric research, and is crucial for understanding the atmospheric dynamics of slow-rotating terrestrial planets such as Venus and Titan (Read & Lebonnois, 2018). The martian atmosphere is also a candidate for super-rotation, as first identified by Lewis and Read (2003).

Global dust storms (GDS) are the most dramatic of all dust-related phenomena in the martian atmosphere, and occur every few martian years. During a GDS, the planet is encircled by a shroud of dust that can persist for several months at a time, drastically affecting the atmospheric state. Such storms have all been observed to occur during the high dust loading season ($L_S = 180^\circ - 360^\circ$), when the planet's orbit brings it closer to the Sun (Kahre et al., 2017). The formation mechanisms of a GDS are still not well understood; in particular, it has not been established why a GDS forms out of regional storms in some years, but not others. Posited hypotheses include the re-distribution of dust between finite reservoirs between years (Mulholland et al., 2013; Newman & Richardson, 2015), competition between the hemispheric circulations during northern winter (Haberle, 1986), weak coupling between orbital and rotational angular momentum on Mars (Newman et al., 2019; Shirley, 2017) and enhanced surface wind stress due to constructive interference of tides (Martinez-Alvarado et al., 2009; Montabone et al., 2008).

© 2021. The Authors.
 This is an open access article under the terms of the [Creative Commons Attribution](https://creativecommons.org/licenses/by/4.0/) License, which permits use, distribution and reproduction in any medium, provided the original work is properly cited.

Lewis and Read (2003) have shown that dust-driven heating can excite a super-rotating jet in the martian atmosphere. In turn, the strengthening of the equatorial jet by the presence of dust affects dust transport; in this way, there is an intimate link between dust-driven heating and the strength of the equatorial jet which may have implications for GDS evolution.

The most recent GDS occurred in Mars Year (MY) 34 (using the naming convention of Clancy et al., 2000). The storm initiated shortly after the northern hemisphere autumn equinox at $L_S = 187^\circ$, and its dynamical evolution was monitored by multiple orbital, surface and Earth-based instruments, for example, (Guzewich et al., 2019; Hernández-Bernal et al., 2019; Kass et al., 2019; Sánchez-Lavega et al., 2019; Shirley et al., 2020; Smith, 2019). Bertrand et al. (2020) simulated the MY34 GDS using the NASA Ames Mars Global Climate Model (MGCM) and noted that eastward tropical expansion was a dominant feature of both the MY25 and MY34 GDS, highlighting the link between super-rotation and dust transport in the early stages of GDS formation. Gillespie et al. (2020) used the EMARS reanalysis to study dust encirclement of the northern hemisphere in the early stages of the GDS, and showed that a significant portion (16%) of the encirclement could be attributed to wind-driven dust advection. Super-rotation during the MY34 GDS was further examined by Montabone et al. (2020), who simulated the GDS period using the MGCM developed at the Laboratoire de Météorologie Dynamique (LMD). They reported a global super-rotation value of $S = 16\%$ during the peak of the MY34 GDS, as compared to a pre-dust storm value of 5% (super-rotation metrics are defined in Section 2.3).

In this study, we perform an analysis of super-rotation during MY33–34, with a special focus on the period leading up to the onset of the MY34 GDS ($L_S = 160^\circ - 187^\circ$) which has not been studied by previous authors. MY33 was used for comparisons as it is an adjacent year that did not have a GDS. For this work, we analyze the outputs from a data assimilation scheme (Lewis et al., 2007) that was used to assimilate temperature and column dust data from the Mars Climate Sounder (MCS) and Atmospheric Chemistry Suite (ACS) instruments into a MGCM. As data assimilation uses observational data to constrain the evolution of model dynamics, it provides an excellent tool to perform such analysis. In Section 2, we describe the satellite observations and give a description of the model and assimilation scheme used. We also introduce metrics to quantify super-rotation. We document our results in Section 3, and discuss our findings in Section 4.

2. Data and Methods

2.1. Observation Data

MCS is a passive 9-channel limb-scanning radiometer aboard the Mars Reconnaissance Orbiter (MRO) (McCleese et al., 2007). Measurements are taken at approximately 3 a.m. and 3 p.m. local time along a Sun-synchronous orbit, across a wavelength range of $0.3 - 45 \mu\text{m}$. Radiance profiles are generated from the surface to around 80 km with an intrinsic vertical resolution of 5 km, enabling the retrieval of profiles of temperature, dust and water ice (Kleinböhl et al., 2009, 2017). We used version v5.2 for all MCS data outside of the MY34 GDS period. During the GDS period ($L_S = 180^\circ - 240^\circ$), v5.3.2 was used instead, as it extracts additional dust information using a far infrared channel centered at 316 cm^{-1} . This is possible in GDS conditions due to the absence of water ice clouds in the lower atmosphere (Kleinböhl et al., 2020; Montabone et al., 2020).

ACS (Korablev et al., 2018) is an array of three infrared spectrometers aboard the ExoMars Trace Gas Orbiter (TGO), that together provide spectral coverage over a wavelength range of $0.7 - 17 \mu\text{m}$. The near-infrared (NIR) channel uses an echelle grating with an Acousto-Optical Tunable filter with a resolving power of 25,000, to retrieve atmospheric density and temperature profiles based on the $1.57 \mu\text{m}$ CO_2 band (Fedorova et al., 2020). The orbit of TGO allows for solar occultations that cross the terminator over a range of local times, a key feature of these datasets. ACS-NIR temperature profiles were included in our assimilation of MY34 over the period $L_S = 163^\circ - 360^\circ$.

2.2. Global Climate Model and Data Assimilation Scheme

The martian atmosphere is modeled using the UK version of the LMD MGCM (Forget et al., 1999). The model utilizes a spectral dynamical core (Hoskins & Simmons, 1975), together with a vertical finite difference

scheme that conserves energy and angular momentum (Simmons & Burridge, 1981) and a semi-Lagrangian tracer advection scheme (Newman et al., 2002). Physical processes on Mars are represented using the physics package from the LMD model, which includes schemes for CO₂ condensation and sublimation, radiative transfer, dust transport, and boundary layer processes (Colaïtis et al., 2013; Forget et al., 1999; Madeleine et al., 2011) amongst many others. Dust transport is via a radiatively active two-moment scheme that advects the dust mass mixing ratio and number density, which are then used to infer the particle size distribution at each point for radiative transfer calculations (Madeleine et al., 2011).

The data assimilation scheme is an implementation of the Analysis Correction (AC) scheme, originally developed for terrestrial applications (Lorenc et al., 1991) and later modified and re-tuned for the martian context (Lewis et al., 1996, 2007). The scheme employs a form of successive corrections, with analysis increments interlaced between dynamical timesteps. It has been successfully employed in assimilating profiles of temperature and column dust opacity from the Thermal Emission Spectrometer (TES) (Lewis & Barker, 2005; Lewis et al., 2007; Montabone et al., 2005) MCS (Holmes et al., 2019, 2020; Steele et al., 2014; Streeter et al., 2020) and ACS (Streeter et al., 2021) instruments.

We performed the assimilation over MY33–34, and ran the model at T42 spatial resolution (triangular truncation at horizontal wavenumber 42), which corresponds to a physical grid resolution of 3.75°. Fifty-five unevenly spaced, terrain-following vertical levels were used, with the model top at approximately 110 km. The water cycle was not simulated, in order to isolate the dynamical impact of the dust. Available temperature profiles from the MCS and ACS instruments were assimilated at each timestep. Dust is advected by model winds, with dust opacity rescaled at each model level to match the total column dust optical depth (CDOD) in the model to MCS observations. Details of the temperature and dust assimilation schemes are given in Lewis et al. (2007) and in the supporting information of Streeter et al. (2020). The inclusion of ACS temperature profiles in the assimilation did not produce any significant changes in the overall structure of the circulation or the strength of the jet during MY34, as compared to an assimilation that only included MCS temperature profiles; this confirms the mutual coherence of the different data sources, and the robustness of the assimilation procedure.

2.3. Super-Rotation Metrics

Super-rotation can be quantified by defining a global super-rotation index S (Lewis & Read, 2003) as

$$S = \frac{\iiint \rho u a \cos \phi dV}{\iiint \rho \Omega a^2 \cos^2 \phi dV} \times 100\%, \quad (1)$$

where ρ is density, u is the zonal wind velocity, and a , ϕ and Ω are the planetary radius, latitude and rotation rate, respectively. The volume element is $dV = a^2 \cos \phi d\lambda d\phi dz$, where λ and z are east longitude and geometric height, respectively. Each integral is performed over the whole atmospheric volume. S is a measure of the ratio between the atmospheric and solid-body components of angular momentum; $S > 0$ only if the atmosphere as a whole has more angular momentum than a pure solid-body rotation.

Super-rotation can also be diagnosed by defining a local super-rotation index s as

$$s = [\bar{m}/\Omega a^2 - 1] \times 100\%. \quad (2)$$

Here \bar{m} is the zonally averaged value of axial angular momentum m , which is defined as

$$m = a \cos \phi [\Omega a \cos \phi + u]. \quad (3)$$

Whereas S measures the global super-rotation, s is a measure of its spatial distribution. s compares the angular momentum of a ring of fluid at a given latitude and height against the angular momentum of an equal-mass fluid ring at rest at the equatorial surface (Read & Lebonnois, 2018). Positive values of s represent super-rotation.

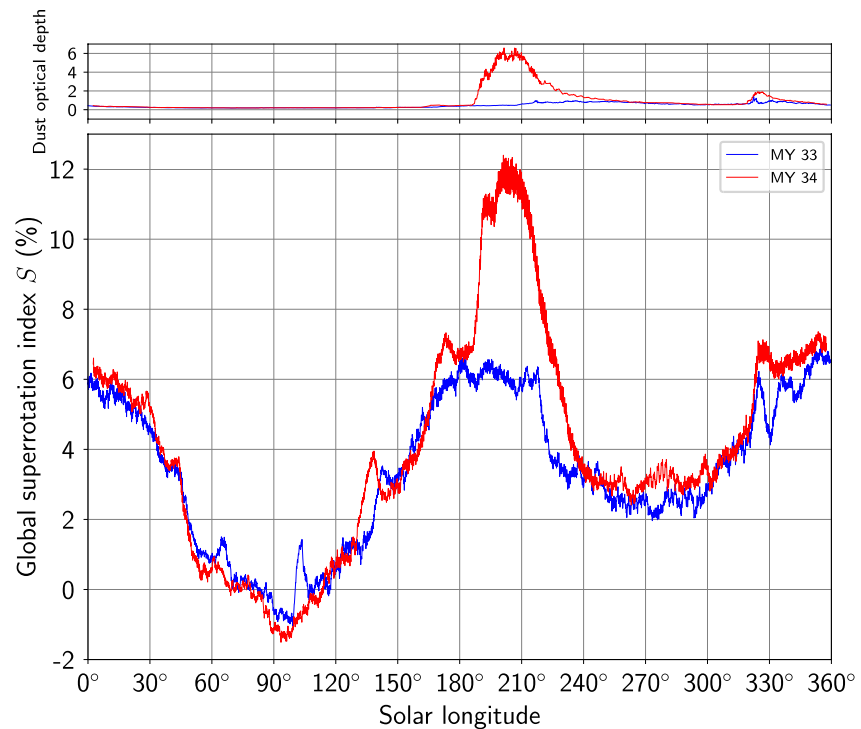


Figure 1. Values of the global super-rotation metric S during Mars Year (MY)33 (blue) and MY34 (red). Positive values indicate global super-rotation. The upper panel shows the corresponding zonal-mean column dust optical depth (CDOD) values averaged over $10^{\circ}\text{N} - 10^{\circ}\text{S}$.

3. Results

3.1. Atmospheric Super-Rotation

Figure 1 shows the variation of the global super-rotation metric S through MY33–34 (lower panel), along with corresponding equatorial (10° CDOD values (upper panel). The large peak in S centered at $L_S = 200^{\circ}$ in MY34 clearly corresponds to the mature phase of the GDS (Kass et al., 2019). There are also several smaller local maxima that occur on both curves. The peaks at $L_S = 105^{\circ}$ in MY33 and $L_S = 135^{\circ}$ in MY34 have been identified as spurious and are due to short absences in MCS data availability over those periods. The MY34 curve has additional peaks at $L_S = 175^{\circ}$ and $L_S = 325^{\circ}$. The peak at $L_S = 175^{\circ}$ occurs just prior to the initiation of the GDS, and will be discussed further in Section 3.3. The peak at $L_S = 325^{\circ}$ corresponds to the timing of the regional storm that occurred late in the year, as can be seen from the concurrent increase in CDOD values.

Outside of the GDS period, the values of S are broadly similar in both years. Global super-rotation variations have a semi-annual structure, with broad peaks occurring during equinoxes and troughs occurring during the solstices. These changes reflect the changes in the Hadley cell structure over the course of the year (Lewis & Read, 2003). S remains largely positive throughout both years of study, except during northern summer solstice. The average values of S are 3.4% and 3.9% for MY33 and MY34, respectively.

3.2. Super-Rotation During the MY34 GDS

The major feature in Figure 1 is a large peak in S corresponding to the mature phase of the MY34 GDS. Global super-rotation in MY34 first diverges significantly from MY33 values at $L_S = 165^{\circ}$ when the dust opacity in the tropics first begins to increase. After an initial peak to $S = 7.2\%$ at $L_S = 173^{\circ}$ global super-rotation increases sharply upon storm onset in the Acidalia corridor at $L_S = 187^{\circ}$. After reaching a plateau at $S = 11.3\%$, the value of S was boosted again by the onset of intense dust lifting in the Tharsis region at $L_S = 197^{\circ}$ (Bertrand et al., 2020; Montabone et al., 2020), reaching a maximum of $S = 12.6\%$ at $L_S = 201^{\circ}$.

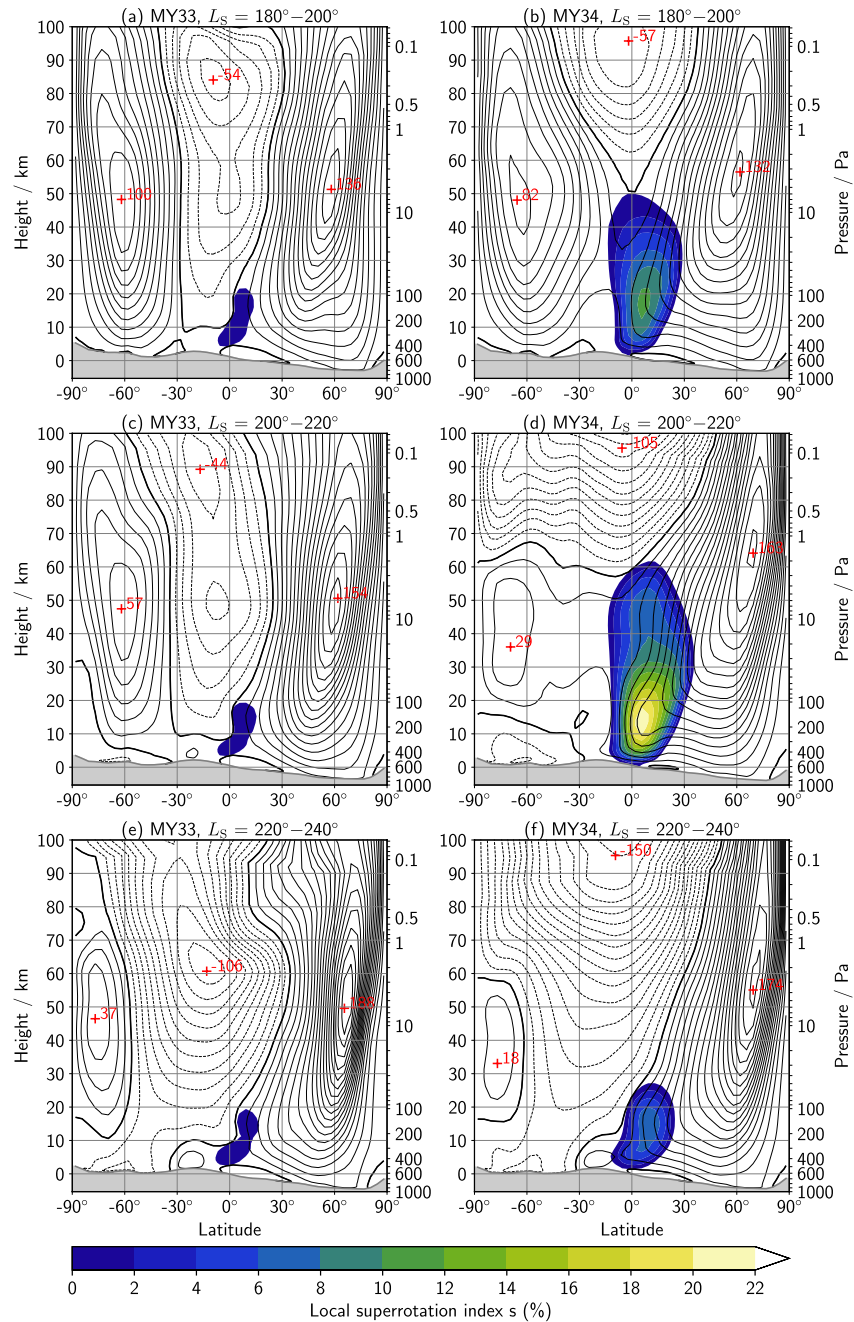


Figure 2. Zonal-mean zonal wind (black contours) and local super-rotation index (filled contours) during the Mars Year (MY)34 global dust storm (GDS) period for MY33 (left) and MY34 (right). Wind contours are drawn at 10 ms^{-1} intervals, with westerlies (easterlies) denoted by solid (dashed) contours. The bold solid contour is the zero wind line. Maximal wind values are marked in red.

The peak value is twice as large as the corresponding MY33 value of $S = 6.2\%$, indicating a significant increase in atmospheric angular momentum. After the peak, S decays at a uniform rate, and returns to background values at $L_S = 240^\circ$

Figure 2 depicts values of zonal-mean zonal winds and the local super-rotation index across latitude and height, during the MY34 GDS period in both years. The data have been averaged in time over 20° periods of solar longitude. These broadly cover the initiation, peak and decay phases of the storm. In all periods, super-rotation is stronger in MY34 than in MY33.

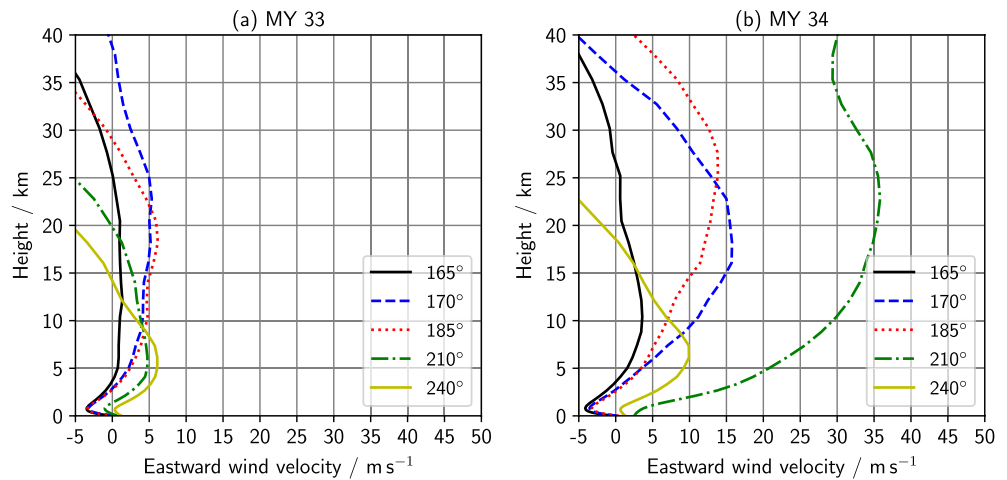


Figure 3. Profiles of tropical zonal-mean zonal winds (averaged diurnally and across 30°S–30°N) for different times during the global dust storm (GDS) period for Mars Year (MY)33 (left) and MY34 (right).

In the time period of storm initiation (Figures 2a and 2b), the atmosphere is in an equinoctial state. There are extratropical westerly jets in both hemispheres, and easterlies over much of the tropics in MY33. There is a substantial difference in tropical wind morphology between the years; this is reflected by the local super-rotation values in the tropics, which peak at $s \approx 12\%$ in MY34 compared to $s \approx 1\%$ in MY33. Tropical westerlies extend up to 50 km in MY34.

Super-rotation is strongest in the period $L_S = 200^\circ - 220^\circ$ of MY34 (Figure 2d), which corresponds to the peak of the GDS. The super-rotating jet continues to dominate the tropical band, and extends up to 60 km. There is a strong peak in local super-rotation of $s = 22\%$ at 15 km, reflecting a significant acceleration of tropical winds by the increased dust presence. Easterly winds above 60 km are also enhanced in MY34, and increase with height to -100 m s^{-1} near the top of the model (although the values above 85 km are also affected by the presence of sponge layers). In comparison, tropical easterly winds in MY33 peak at -40 m s^{-1} at 50 km, and remain relatively constant at higher altitudes (Figure 2c).

In the decay phase of the storm (Figures 2e and 2f), easterly winds dominate the tropical regions above 20 km and increase monotonically in MY34 to a peak of -140 m s^{-1} . Super-rotation is confined to the lower atmosphere below 30 km, and is greatly reduced in intensity.

Figure 3 shows the evolution of zonal-mean zonal wind profiles in the tropics over the course of the GDS period for MY33 (left) and MY34 (right). Wind profiles at each solar longitude were averaged diurnally and between 30°S and 30°N.

The tropical zonal wind profile does not change substantially between $L_S = 165^\circ$ and 210° of MY33. Easterly winds in the lowermost atmosphere are overlain by westerly winds with velocities of around 5 m s^{-1} (Figure 3a). The wind profile for $L_S = 165^\circ$ in MY34 is similar to the winds in MY33, but by $L_S = 170^\circ$ zonal wind speeds have increased at almost all heights (Figure 3b). The wind profile weakens slightly at $L_S = 185^\circ$ before strengthening substantially to reach peak values of 35 m s^{-1} at $L_S = 210^\circ$ with westerly winds penetrating all the way down to the lowest model level (5 m above the surface). In the decay phase of the GDS period, wind profiles from MY34 weaken and start to converge with profiles from MY33.

3.3. Atmospheric Circulation Prior to GDS Onset

Figure 4 shows the evolution of the meridional circulation and the dust distribution in the assimilation for both years over the period $L_S = 158^\circ - 185^\circ$ prior to GDS initiation at $L_S = 187^\circ$. There are no substantive differences between the years at $L_S = 158^\circ$ (Figures 4a and 4b). At $L_S = 161^\circ$ in MY34 there is significant dust lifting in the southern hemisphere, starting around 50° and spreading equatorward. Some of this dust is entrained into the Hadley cell circulation and is transported to higher levels in the atmosphere (Figure 4d).

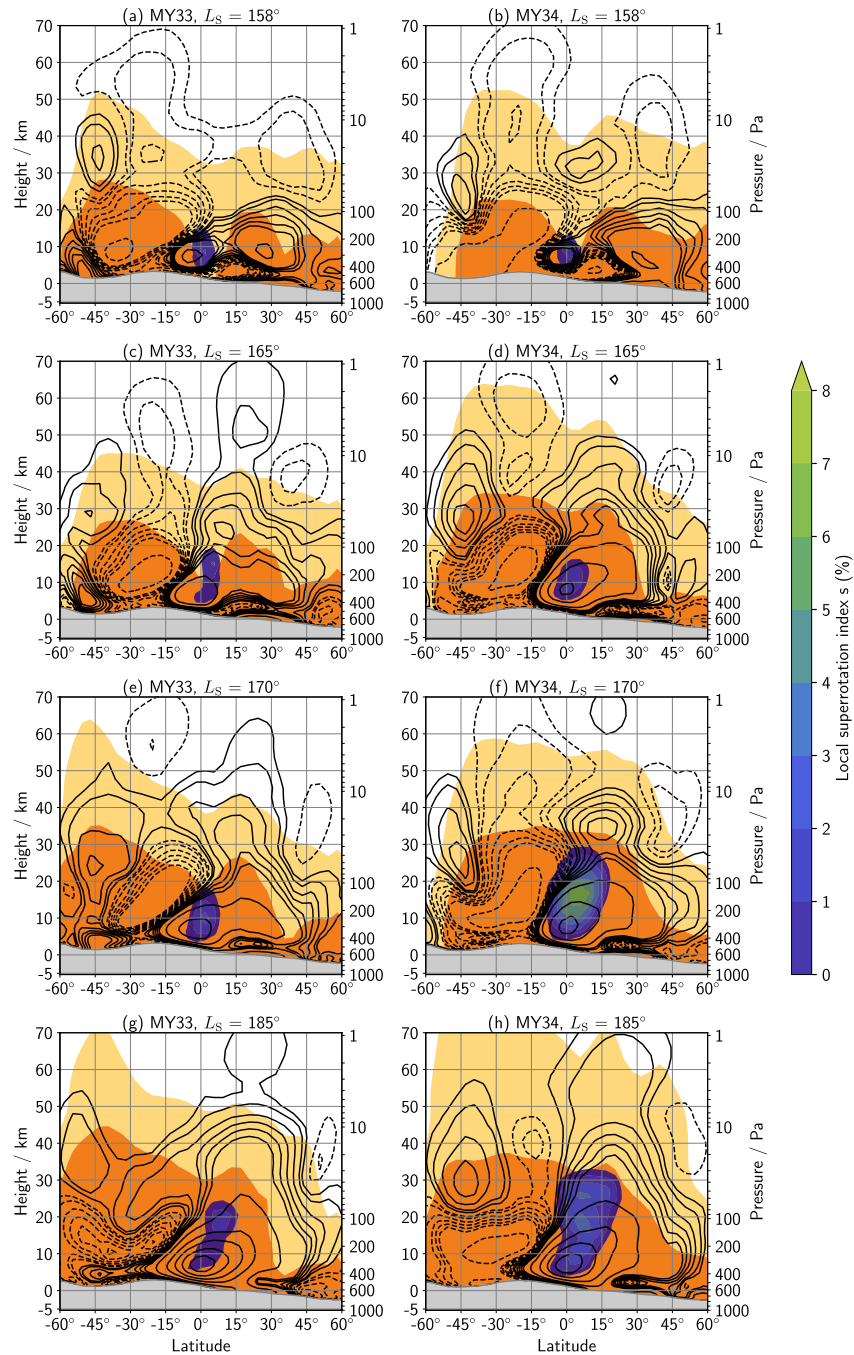


Figure 4. Zonal-mean dust distribution and dynamical structure at four times (rows) in the lead-up to the global dust storm (GDS) for Mars Year (MY)33 (left) and MY34 (right). Light (dark) orange shading shows regions of greater than 1×10^8 (3×10^8) dust particles per kg. Blue-green filled contours indicate the local super-rotation index. Solid (dashed) lines show positive (negative) contours of the mass streamfunction, drawn at $\pm(0.5, 1, 2, 3, 4, 5, 10, 20, 30, 40, 50) \times 10^8 \text{ kg m}^{-1} \text{ s}^{-1}$.

The resulting dust distribution is more uniformly spread across tropical latitudes compared to MY33, where the bulk of the dust remains in the southern mid-latitudes (Figure 4c).

The impact of the different dust distributions on the circulation can be seen in Figures 4e–4h. In MY33, dust-driven heating is enhanced in the southern mid-latitudes compared to the tropics, causing an inversion of the diabatic heating gradient in the southern hemisphere between 20 and 40 km. This weakens the

thermally direct circulation in the southern hemisphere (Holton, 2004), resulting in the formation of a lop-sided Hadley cell with a wavy upwelling branch that is less efficient at vertical tracer transport (Figures 4e and 4g). In contrast, the relatively uniform dust distribution in MY34 engenders a symmetrical Hadley cell with an upwelling branch closely aligned to the vertical, as well as enhanced local super-rotation (Figures 4f and 4h). The circulation patterns in both years do not change substantially between $L_S = 170^\circ$ and 185° suggesting that they are relatively stable.

4. Discussion

Our MGCM with data assimilation predicted a peak value of $S = 12.6\%$ during the peak of the storm in MY34, as compared to a value of $S = 6.3\%$ in MY33 (Figure 1). While the findings are qualitatively similar to those of Montabone et al. (2020), our results show that super-rotation increased by a factor of two during the GDS, rather than by a factor of 3 as found by Montabone et al. (2020). This quantitative difference could be due to differences in the vertical distribution of dust; for example, Guzewich et al. (2013) have shown that tropical lower atmospheric temperatures are sensitive to different dust profiles, which can lead to $10 - 20 \text{ ms}^{-1}$ changes in westerly jet strength. Although the vertical dust profile is not directly constrained by observations in our model, the vertical distribution of dust heating is still captured via the assimilation of vertical temperature profiles; this constraint provides greater confidence in the resulting wind speeds. Climatological super-rotation values are also lower in the assimilation as compared to the free-running model: annual-mean values of S are 3.4% and 3.9% for MY33 and MY34, respectively, compared to $S = 4.5\% - 5.8\%$ as found by Lewis and Read (2003) who used the same model under different dust loading scenarios, without assimilation.

The morphology of tropical winds in our model during the GDS (Figure 2) is consistent with the dust-driven enhancement of thermal tides, as explained by Lewis and Read (2003). As westward-propagating tides are excited by dust in the lower atmosphere they propagate vertically and induce westerly super-rotating winds at their source regions (Fels & Lindzen, 1974). Furthermore, the tides eventually break in the upper atmosphere and deposit easterly momentum into the background winds, resulting in strengthened easterly flow at higher levels. Such tidally driven changes in upper atmospheric winds will have a significant impact on the distribution of trace species such as water that are transported into the upper atmosphere during GDSs (Aoki et al., 2019; Fedorova et al., 2018, 2020). By triggering the breaking levels of gravity waves, these winds also play a role in controlling the amplitude and spectral distribution of gravity waves entering the thermosphere, which has implications for water loss as enhanced gravity wave activity increases the hydrogen escape flux (Yigit et al., 2021).

Enhanced tropical winds played a significant role in the horizontal transport and distribution of dust during the initial phase of the GDS (Bertrand et al., 2020; Gillespie et al., 2020). We have shown that the martian atmosphere in MY34 was already in a state of enhanced super-rotation prior to the onset of the GDS at $L_S = 187^\circ$ (Figures 1, 2d, 3 and 4f). One consequence of strengthened pre-GDS tropical winds is that eastward dust advection during the initial stages of the GDS would have been more rapid in MY34 than in years with weaker pre-storm super-rotation. This rapid transport would have enabled the timely activation of the secondary Tharsis lifting center, which was crucial in making the dust storm global in extent (Bertrand et al., 2020; Montabone et al., 2020). Furthermore, we observe that super-rotating winds create regions of enhanced vertical wind shear in the lower atmosphere (Figure 3b). As strongly sheared winds are subject to Kelvin-Helmholtz instability, we speculate that jet-induced wind shear could have enhanced the generation of turbulence and surface wind stresses prior to the storm. This would lead to enhanced dust lifting, especially in the daytime when atmospheric static stability is low. However, further work will be required to quantify the impact of such shear-induced turbulence on vertical dust transport.

Our analysis of the pre-storm circulation indicates that dust lifting in the southern tropical regions played a key role in inducing the circulation pattern of a symmetric Hadley cell with a vertically aligned tropical upwelling branch (Figure 4). As a result of this pattern, vertical transport was much more efficient in MY34 in the lead-up to the storm, as compared to MY33. Such a pre-storm circulation pattern could be an important pre-requisite condition that enabled the rapid lifting of dust during GDS initiation (Haberle et al., 1993; Shirley et al., 2020; Wilson et al., 2008). Therefore, even though the MY34 GDS is considered to

have initiated in the northern hemisphere (Bertrand et al., 2020; Sánchez-Lavega et al., 2019), our results indicate that dust lifting in the southern hemisphere may still have played a crucial role in GDS initiation.

Data Availability Statement

Assimilation data from this study may be accessed at <https://doi.org/10.21954/ou.rd.13332455>. ACS raw data products are available from the ESA Planetary Science Archive (<https://archives.esac.esa.int/psa/>). MCS data v5.3.2 was used during the MY34 GDS period, and is described in Kleinböhl et al. (2020). MCS data v5.2.9 was used outside of the GDS period, and is available from the NASA Planetary Data System (<https://pds-atmospheres.nmsu.edu/>).

Acknowledgments

K. Rajendran, S. R. Lewis, J. A. Holmes, P. M. Streeter, and M. R. Patel acknowledge the support of the UK Space Agency under the following grants: ST/R00145X/1 (K. Rajendran, S. R. Lewis, and M. R. Patel), ST/S001405/1 (J. A. Holmes, S. R. Lewis, and M. R. Patel), ST/V005332/1 (P. M. Streeter, S. R. Lewis, and M. R. Patel) and ST/V002295/1 (M. R. Patel). A. A. Fedorova acknowledges the subsidy of the Ministry of Science and Higher Education of the Russian Federation to IKI RAS (theme 'Planeta'). P. M. Streeter acknowledges the support of the UK Science and Technology Facilities Council under grant ST/N50421X/1, and the Open University in the form of a PhD studentship.

References

- Aoki, S., Vandaele, A., Daerden, F., Villanueva, G., Luzzi, G., Thomas, I., et al. (2019). Water vapor vertical profiles on mars in dust storms observed by TGO/NOMAD. *Journal of Geophysical Research: Planets*, 124(12), 3482–3497. <https://doi.org/10.1029/2019je006109>
- Bertrand, T., Wilson, J., Kahre, M., Urata, R., & Kling, A. (2020). Simulation of the 2018 global dust storm on mars using the NASA AMES mars GCM: A multi-tracer approach. *Journal of Geophysical Research: Planets*, e2019JE006122. <https://doi.org/10.1029/2019je006122>
- Clancy, R., Sandor, B., Wolff, M., Christensen, P., Smith, M., Pearl, J., & Wilson, R. (2000). An intercomparison of ground-based millimeter, MGS TES, and viking atmospheric temperature measurements: Seasonal and interannual variability of temperatures and dust loading in the global mars atmosphere. *Journal of Geophysical Research*, 105(E4), 9553–9571. <https://doi.org/10.1029/1999je001089>
- Colaïtis, A., Spiga, A., Hourdin, F., Rio, C., Forget, F., & Millour, E. (2013). A thermal plume model for the martian convective boundary layer. *Journal of Geophysical Research: Planets*, 118(7), 1468–1487. <https://doi.org/10.1002/jgre.20104>
- Fedorova, A., Bertaux, J., Betsis, D., Montmessin, F., Korablev, O., Maltagliati, L., & Clarke, J. (2018). Water vapor in the middle atmosphere of mars during the 2007 global dust storm. *Icarus*, 300, 440–457. <https://doi.org/10.1016/j.icarus.2017.09.025>
- Fedorova, A., Montmessin, F., Korablev, O., Luginin, M., Trokhimovskiy, A., Belyaev, D., et al. (2020). Stormy water on mars: The distribution and saturation of atmospheric water during the dusty season. *Science*, 367(6475), 297–300. <https://doi.org/10.1126/science.aay9522>
- Fels, S., & Lindzen, R. (1974). The interaction of thermally excited gravity waves with mean flows. *Geophysical & Astrophysical Fluid Dynamics*, 6(2), 149–191. <https://doi.org/10.1080/03091927409365793>
- Forget, F., Hourdin, F., Fournier, R., Hourdin, C., Talagrand, O., Collins, M., et al. (1999). Improved general circulation models of the martian atmosphere from the surface to above 80 km. *Journal of Geophysical Research*, 104(E10), 24155–24175. <https://doi.org/10.1029/1999je001025>
- Gillespie, H., Greybush, S., & Wilson, R. (2020). An investigation of the encirclement of mars by dust in the 2018 global dust storm using emars. *Journal of Geophysical Research: Planets*, 125(7), e2019JE006106. <https://doi.org/10.1029/2019je006106>
- Guzewich, S., Lemmon, M., Smith, C., Martinez, G., de Vicente-Retortillo, Á., Newman, C., et al. (2019). Mars science laboratory observations of the 2018/mars year 34 global dust storm. *Geophysical Research Letters*, 46(1), 71–79. <https://doi.org/10.1029/2018gl080839>
- Guzewich, S., Toigo, A., Richardson, M., Newman, C., Talaat, E., Waugh, D., & McConnochie, T. (2013). The impact of a realistic vertical dust distribution on the simulation of the martian general circulation. *Journal of Geophysical Research: Planets*, 118(5), 980–993. <https://doi.org/10.1002/jgre.20084>
- Haberle, R. (1986). Interannual variability of global dust storms on mars. *Science*, 234(4775), 459–461. <https://doi.org/10.1126/science.234.4775.459>
- Haberle, R., Pollack, J., Barnes, J., Zurek, R., Leovy, C., Murphy, J., & Schaeffer, J. (1993). Mars atmospheric dynamics as simulated by the NASA AMES general circulation model: 1. The zonal-mean circulation. *Journal of Geophysical Research*, 98(E2), 3093–3123. <https://doi.org/10.1029/92je02946>
- Hernández-Bernal, J., Sánchez-Lavega, A., del Río-Gaztelurrutia, T., Hueso, R., Cardesín-Moinelo, A., Ravanis, E., & Wood, S. (2019). The 2018 martian global dust storm over the south polar region studied with mex/VMC. *Geophysical Research Letters*, 46(17–18), 10330–10337.
- Hide, R. (1969). Dynamics of the atmospheres of the major planets with an appendix on the viscous boundary layer at the rigid bounding surface of an electrically-conducting rotating fluid in the presence of a magnetic field. *Journal of the Atmospheric Sciences*, 26(5), 841–853. [https://doi.org/10.1175/1520-0469\(1969\)026<0841:dotaat>2.0.co;2](https://doi.org/10.1175/1520-0469(1969)026<0841:dotaat>2.0.co;2)
- Holmes, J., Lewis, S., & Patel, M. (2020). Openmars: A global record of martian weather from 1999–2015. *Planetary and Space Science*, 104962.
- Holmes, J., Lewis, S., Patel, M., & Smith, M. (2019). Global analysis and forecasts of carbon monoxide on mars. *Icarus*, 328, 232–245. <https://doi.org/10.1016/j.icarus.2019.03.016>
- Holton, J. (2004). *An introduction to dynamic meteorology*. Elsevier Academic Press.
- Hoskins, B., & Simmons, A. (1975). A multi-layer spectral model and the semi-implicit method. *The Quarterly Journal of the Royal Meteorological Society*, 101(429), 637–655. <https://doi.org/10.1002/qj.49710142918>
- Kahre, M., Murphy, J., Newman, C., Wilson, R., Cantor, B., Lemmon, M., & Wolff, M. (2017). The mars dust cycle. In R. Haberle, R. Clancy, F. Forget, M. Smith, & R. Zurek (Eds.), *The atmosphere and climate of mars* (pp. 295–337). Cambridge University Press. <https://doi.org/10.1017/9781139060172.010>
- Kass, D., Schofield, J., Kleinböhl, A., McCleese, D., Heavens, N., Shirley, J., & Steele, L. (2019). Mars climate sounder observation of mars' 2018 global dust storm. *Geophysical Research Letters*, 47(23), e2019GL083931.
- Kleinböhl, A., Friedson, A., & Schofield, J. (2017). Two-dimensional radiative transfer for the retrieval of limb emission measurements in the martian atmosphere. *Journal of Quantitative Spectroscopy and Radiative Transfer*, 187, 511–522. <https://doi.org/10.1016/j.jqsrt.2016.07.009>
- Kleinböhl, A., Schofield, J., Kass, D., Abdou, W., Backus, C., Sen, B., et al. (2009). Mars climate sounder limb profile retrieval of atmospheric temperature, pressure, and dust and water ice opacity. *Journal of Geophysical Research*, 114(E10). <https://doi.org/10.1029/2009je003358>

- Kleinböhl, A., Spiga, A., Kass, D., Shirley, J., Millour, E., Montabone, L., & Forget, F. (2020). Diurnal variations of dust during the 2018 global dust storm observed by the mars climate sounder. *Journal of Geophysical Research: Planets*, 125(1). <https://doi.org/10.1029/2019je006115>
- Korablev, O., Montmessin, F., Trokhimovskiy, A., Fedorova, A., Shakun, A., Grigoriev, A., et al. (2018). The atmospheric chemistry suite (ACS) of three spectrometers for the exomars 2016 trace gas orbiter. *Space Science Reviews*, 214(1), 7.
- Lewis, S., & Barker, P. (2005). Atmospheric tides in a mars general circulation model with data assimilation. *Advances in Space Research*, 36(11), 2162–2168. <https://doi.org/10.1016/j.asr.2005.05.122>
- Lewis, S., & Read, P. (2003). Equatorial jets in the dusty martian atmosphere. *Journal of Geophysical Research*, 108(E4). <https://doi.org/10.1029/2002je001933>
- Lewis, S., Read, P., & Collins, M. (1996). Martian atmospheric data assimilation with a simplified general circulation model: Orbiter and lander networks. *Planetary and Space Science*, 44(11), 1395–1409. [https://doi.org/10.1016/s0032-0633\(96\)00058-x](https://doi.org/10.1016/s0032-0633(96)00058-x)
- Lewis, S., Read, P., Conrath, B., Pearl, J., & Smith, M. (2007). Assimilation of thermal emission spectrometer atmospheric data during the mars global surveyor aerobraking period. *Icarus*, 192(2), 327–347. <https://doi.org/10.1016/j.icarus.2007.08.009>
- Lorenc, A., Bell, R., & Macpherson, B. (1991). The meteorological office analysis correction data assimilation scheme. *The Quarterly Journal of the Royal Meteorological Society*, 117(497), 59–89. <https://doi.org/10.1002/qj.49711749704>
- Madeleine, J., Forget, F., Millour, E., Montabone, L., & Wolff, M. (2011). Revisiting the radiative impact of dust on mars using the LMD global climate model. *Journal of Geophysical Research*, 116(E11). <https://doi.org/10.1029/2011je003855>
- Martinez-Alvarado, O., Montabone, L., Lewis, S., Moroz, I., & Read, P. (2009). Transient teleconnection event at the onset of a planet-encircling dust storm on mars. *Annals of Geophysics*, 27(9), 3663–3676. <https://doi.org/10.5194/angeo-27-3663-2009>
- McCleese, D., Schofield, J., Taylor, F., Calcutt, S., Foote, M., Kass, D., & Zurek, R. (2007). Mars climate sounder: An investigation of thermal and water vapor structure, dust and condensate distributions in the atmosphere, and energy balance of the polar regions. *Journal of Geophysical Research*, 112(E5). <https://doi.org/10.1029/2006je002790>
- Montabone, L., Lewis, S., & Read, P. (2005). Interannual variability of martian dust storms in assimilation of several years of mars global surveyor observations. *Advances in Space Research*, 36(11), 2146–2155. <https://doi.org/10.1016/j.asr.2005.07.047>
- Montabone, L., Martinez-Alvarado, O., Lewis, S., Read, P., & Wilson, R. (2008). Teleconnection in the martian atmosphere during the 2001 planet-encircling dust storm. In *Third International Workshop on the Mars Atmosphere: Modeling and Observations* (Vol. 1447, p. 9077).
- Montabone, L., Spiga, A., Kass, D., Kleinböhl, A., Forget, F., & Millour, E. (2020). Martian year 34 column dust climatology from mars climate sounder observations: Reconstructed maps and model simulations. *Journal of Geophysical Research: Planets*, e2019JE006111. <https://doi.org/10.1029/2019je006111>
- Mulholland, D., Read, P., & Lewis, S. (2013). Simulating the interannual variability of major dust storms on mars using variable lifting thresholds. *Icarus*, 223(1), 344–358. <https://doi.org/10.1016/j.icarus.2012.12.003>
- Newman, C., Lee, C., Mischna, M., Richardson, M., & Shirley, J. (2019). An initial assessment of the impact of postulated orbit-spin coupling on mars dust storm variability in fully interactive dust simulations. *Icarus*, 317, 649–668. <https://doi.org/10.1016/j.icarus.2018.07.023>
- Newman, C., Lewis, S., Read, P., & Forget, F. (2002). Modeling the martian dust cycle, 1. Representations of dust transport processes. *Journal of Geophysical Research*, 107(E12), 6–1–6–18. <https://doi.org/10.1029/2002je001910>
- Newman, C., & Richardson, M. (2015). The impact of surface dust source exhaustion on the martian dust cycle, dust storms and interannual variability, as simulated by the marswrf general circulation model. *Icarus*, 257, 47–87. <https://doi.org/10.1016/j.icarus.2015.03.030>
- Read, P. (1986). Super-rotation and diffusion of axial angular momentum: I. 'Speed limits' for axisymmetric flow in a rotating cylindrical fluid annulus. *The Quarterly Journal of the Royal Meteorological Society*, 112(471), 231–251. <https://doi.org/10.1256/smsqj.47112>
- Read, P., & Lebonnois, S. (2018). Superrotation on Venus, on titan, and elsewhere. *Annual Review of Earth and Planetary Sciences*, 46, 175–202. <https://doi.org/10.1146/annurev-earth-082517-010137>
- Sánchez-Lavega, A., del Río-Gaztelurrutia, T., Hernández-Bernal, J., & Delcroix, M. (2019). The onset and growth of the 2018 martian global dust storm. *Geophysical Research Letters*, 46(11), 6101–6108.
- Shirley, J. (2017). Orbit-spin coupling and the circulation of the martian atmosphere. *Planetary and Space Science*, 141, 1–16. <https://doi.org/10.1016/j.pss.2017.04.006>
- Shirley, J., Kleinböhl, A., Kass, D., Steele, L., Heavens, N., Suzuki, S., & McCleese, D. (2020). Rapid expansion and evolution of a regional dust storm in the acidalia corridor during the initial growth phase of the martian global dust storm of 2018. *Geophysical Research Letters*, 47(9), e2019GL084317. <https://doi.org/10.1029/2019gl084317>
- Simmons, A., & Burridge, D. (1981). An energy and angular-momentum conserving vertical finite-difference scheme and hybrid vertical coordinates. *Monthly Weather Review*, 109(4), 758–766. [https://doi.org/10.1175/1520-0493\(1981\)109<0758:aeaamc>2.0.co;2](https://doi.org/10.1175/1520-0493(1981)109<0758:aeaamc>2.0.co;2)
- Smith, M. (2019). Themis observations of the 2018 mars global dust storm. *Journal of Geophysical Research: Planets*, 124(11), 2929–2944. <https://doi.org/10.1029/2019je006107>
- Steele, L., Lewis, S., Patel, M., Montmessin, F., Forget, F., & Smith, M. (2014). The seasonal cycle of water vapour on mars from assimilation of thermal emission spectrometer data. *Icarus*, 237, 97–115. <https://doi.org/10.1016/j.icarus.2014.04.017>
- Streeter, P., Lewis, S., Patel, M., Holmes, J., Fedorova, A., Kass, D., & Kleinböhl, A. (2021). Asymmetric impacts on mars' polar vortices from an equinoctial global dust storm. *Journal of Geophysical Research: Planets*, e2020JE006774. <https://doi.org/10.1029/2020je006774>
- Streeter, P., Lewis, S., Patel, M., Holmes, J., & Kass, D. (2020). Surface warming during the 2018/mars year 34 global dust storm. *Geophysical Research Letters*, 47(9), e2019GL083936. <https://doi.org/10.1029/2019gl083936>
- Wilson, R., Haberle, R., Noble, J., Bridger, A., Schaeffer, J., Barnes, J., & Cantor, B. (2008). Simulation of the 2001 planet-encircling dust storm with the NASA/NOAA mars general circulation model. In *Third International Workshop on the Mars Atmosphere: Modeling and Observations* (Vol. 1447, p. 9023).
- Yigit, E., Medvedev, A., Benna, M., & Jakosky, B. (2021). Dust storm-enhanced gravity wave activity in the martian thermosphere observed by maven and implication for atmospheric escape. *Geophysical Research Letters*, 48(5), e2020GL092095.